Title Page:

Title: Diffusion Histology Imaging Detects and Classifies Glioblastoma Pathology Missed by Conventional Magnetic Resonance Imaging

Running title: Detection and Classification of Glioblastoma Pathology

Authors: Zezhong Ye[1], Richard L. Price[2], Xiran Liu[3*], Joshua Lin[1‡], Qingsong Yang[4], Peng Sun[1], Anthony Wu[5], Liang Wang[3], Rowland Han[2], Chunyu Song[5], Ruimeng Yang[6], Sam E. Gary[7], Diane D. Mao[2], Michael Wallendorf[8], Jian L. Campian[9], Jr-Shin Li[3], Sonika Dahiya[10†], Albert H. Kim[2†], and Sheng-Kwei Song[1]

Affiliations:

[1]Department of Radiology, Washington University School of Medicine, St. Louis, MO 63110

[2]Department of Neurological Surgery, Washington University School of Medicine, St. Louis, MO 63110

[3]Department of Electrical & System Engineering, Washington University, St. Louis, MO 63130

[4]Department of Radiology, Changhai Hospital, Shanghai 200433, China

[5]Department of Biomedical Engineering, Washington University, St. Louis, MO 63130

[6]Department of Radiology, Guangzhou First People's Hospital, School of Medicine, South China University of Technology, Guangzhou, Guangdong 510180, China

[7]Medical Scientist Training Program, The University of Alabama at Birmingham, Birmingham, AL 35294

[8]Department of Biostatistics, Washington University School of Medicine, St. Louis, MO 63110

[9]Department of Medicine, Division of Oncology, Washington University School of Medicine, St. Louis, MO 63110

[10]Department of Pathology and Immunology, Washington University School of Medicine, St. Louis, MO 63110

Corresponding Authors:

Albert H. Kim, MD, PhD

Department of Neurological Surgery, Washington University School of Medicine,

Campus Box 8057, 660 S. Euclid Avenue, St. Louis, MO 63110, USA

Tel: +1 314-747-6561

Fax: +1 314-362-2107

Email address: alberthkim@wustl.edu

Sonika Dahiya, MD

Department of Pathology and Immunology, Washington University School of Medicine,

660 S. Euclid Avenue, St. Louis, MO 63110, USA

Tel: +1 314-362-7684

Fax: +1 314-362-7765

Email address: sdahiya@wustl.edu

*Current Address: Institute of Computational and Mathematical Engineering, Stanford University, Palo Alto, CA 94305, USA

‡ Current Address: Keck School of Medicine, University of Southern California, Los Angeles, CA 90033, USA

Funding: This work was supported in part by National Institutes of Health (R01-NS047592, P01-NS059560 and U01-EY025500 to S.-K.S., R01NS094670 to A.H.K.), The Christopher Davidson and Knight Family Fund (A.H.K.), the Duesenberg Research Fund (A.H.K.), National Multiple Sclerosis Society (RG 5258-A-5 and RG 1701-26617 to S.-K.S.), The Fundamental Research Funds for the Central Universities (SCUT 2018MS23 to R.Y.) and the Natural Science Foundation of Guangdong Province in China (2018A030313282 to R.Y).

Conflict of Interest: A.H.K. has received research grants from Monteris Medical and Stryker, both of which have no direct relation to the current study. The other authors declare no conflict of interests.

Authorship: Z.Y., A.H.K., S.-K.S. and S.D. wrote the paper, and were assisted by J.L., R.H. and S.E.G. Z.Y., R.L.P. and D.D.M. performed the experiments. Z.Y., P.S., A.G., R.Y. and C.S. analyzed the experimental data. S.D. performed pathological evaluations. X.L., L.W. Z.Y. and J.-S.L. developed the classifier. M.W. conducted the statistical analyses. A.H.K., R.P. provided surgical specimens for imaging. S.-K.S., A.H.K., and S.D. oversaw the project. All authors have reviewed and approved the final version of the manuscript.

Total Manuscript Word Count: 5999

Abstract

Background

Glioblastoma (GBM) is one of the deadliest cancers with no cure. While conventional MRI has been widely adopted for examining GBM clinically, accurate neuroimaging assessment of tumor histopathology for improved diagnosis, surgical planning, and treatment evaluation, remains an unmet need in the clinical management of GBMs.

Methods

We employ a novel Diffusion Histology Imaging (DHI) approach, combining diffusion basis spectrum imaging (DBSI) and machine learning, to detect, differentiate, and quantify areas of high cellularity, tumor necrosis, and tumor infiltration in GBM.

Results

Gd-enhanced T1W or hyper-intense FLAIR failed to reflect the morphological complexity underlying tumor in GBM patients. Contrary to the conventional wisdom that apparent diffusion coefficient (ADC) negatively correlates with increased tumor cellularity, we demonstrate disagreement between ADC and histologically confirmed tumor cellularity in glioblastoma specimens, whereas DBSI-derived restricted isotropic diffusion fraction positively correlated with tumor cellularity in the same specimens. By incorporating DBSI metrics as classifiers for a supervised machine learning algorithm, we accurately predicted high tumor cellularity, tumor necrosis, and tumor infiltration with 87.5%, 89.0% and 93.4% accuracy, respectively.

Conclusion

Our results suggest that DHI might serve as a favorable alternative to current neuroimaging techniques for guiding biopsy or surgery as well as monitoring therapeutic response in the treatment of glioblastoma.

Keywords: Glioblastoma, Magnetic Resonance Imaging, Diffusion Histology Imaging, Brain Tumor Pathology

Key Points

1. Clinical MRI lacks specificity and sensitivity in detecting morphological features in GBM.

2. DBSI-derived morphological metrics reflect tumor cellularity, necrosis, and white matter tracts.

3. DHI predicts and classifies key histopathological features of GBM.

Importance of the Study

Current clinical diagnosis, surgical resection planning, and assessment of treatment response for GBM patients relies heavily on gadolinium enhanced T1-weighted MRI, despite the enhancement is non-specific to tumor growth merely reflecting a disrupted blood-brain barrier. The complex tumor microenvironment and spatial heterogeneity make GBM very difficult to characterize using current clinical imaging modalities. In this study, we developed a novel imaging technique to characterize key histological features of GBM to accurately predict high tumor cellularity, tumor necrosis, and tumor infiltration. Current proof-of-concept approach if validated in a larger cohort of GBM patients could provide a solution resolve issues such as pseudoprogression and radiation necrosis currently plague neuroimaging modalities to assess GBM in living patients.

Text:

Introduction

Glioblastoma (GBM) is the most common primary malignant brain tumor in adults.[1] It is estimated that 13310 new GBM cases will be diagnosed during 2019 in the U.S.[1] Despite extensive multimodality treatment; including surgical resection, chemotherapy, and radiation; patients with GBM exhibit a dismal 5-year survival rate of 5.5%.[1] Histologically, GBMs are characterized by increased cellularity, vascular proliferation, necrosis, and infiltration into normal brain parenchyma.[2] However, currently, the histopathological complexity of GBM cannot be fully appreciated without microscopic examination of tumor specimens.

Gadolinium (Gd)-enhanced T1-weighted MRI (T1WI) is the standard clinical imaging modality for detection, surgical planning, and evaluation of GBM treatment response.[3-6] Contrast-enhancement in T1W images is clinically interpreted as a measure of tumor burden and is widely used as the target for surgical resection.[6] However, due to the infiltrative nature of GBM, tumor cells are known to extend well beyond the area of contrast enhancement.[3] After treatment, contrast enhancement is not diagnostically specific for GBM since it reflects not only increased Gd leakage due to angiogenesis induced by malignant tumors but also blood-brain barrier disruption triggered by other factors, including radiation effects and ischemia.[7-9] Therefore, Gd enhancement does not accurately measure tumor burden nor specifically reflect various pathological changes.

Conventional MR sequences such as T2-weighted imaging (T2WI) and fluid-attenuated inversion recovery (FLAIR) imaging have also been employed to localize non-enhancing tumor to complement Gd-enhanced T1WI. The combination of these imaging sequences was adopted into the Response Assessment in Neuro-Oncology (RANO).[3] However, precisely quantifying the increase in T2WI/FLAIR signal intensity remains difficult. Differentiating non-enhancing tumor

from other causes of increased T2WI or FLAIR signal intensity, such as edema, radiation effect, ischemic injury, postoperative changes, or other treatment effects, continues to challenge clinicians.

In addition to conventional T1WI and T2WI, diffusion-weighted imaging (DWI) and the derived apparent diffusion coefficient (ADC) have been employed to detect and assess tumor cellularity in many cancers based on the hypothesis that increased tumor cellularity restricts diffusion, leading to decreased ADC values.[10] ADC has been shown to decrease with increasing glioma grade[11] and applied to characterize the infiltrative pattern of recurrent tumor after treatment.[12] However, ADC loses specificity and sensitivity in the presence of co-existing necrosis (increased ADC), tumor infiltration (decreased ADC) and/or vasogenic edema (increased ADC), complicating local brain diffusion characteristics. Combining multiple MR sequences falls short of predicting the complex and heterogeneous GBM tumor microenvironment. Additionally, the gold standard of surgical biopsy carries risk. Thus the development of noninvasive alternatives to decipher the complex GBM tumor histopathology is urgently needed so that clinicians can make rational decisions about continuing, stopping, or changing treatments.

Diffusion basis spectrum imaging (DBSI) utilizes a data-driven multiple-tensor modeling approach to differentiate coexisting morphological features resulting from tumor pathologies or other attributes within an image voxel. We have previously demonstrated that DBSI quantifies tissue injury in an array of central nervous system disorders including multiple sclerosis,[13] cervical spondylotic myelopathy,[14] and epilepsy.[15] In this study, we demonstrate both Gd-enhanced T1WI and hyperintense FLAIR areas contain a spectrum of DBSI-derived morphological signatures in GBM. Using a modified DBSI algorithm to separate inflammation from tumor cellularity, we show DBSI-derived restricted-isotropic-diffusion fraction positively correlated with tumor cellularity in

GBM specimens. Finally, to improve the performance of a DBSI-based approach, we developed a more sophisticated and robust Diffusion Histology Imaging (DHI) approach, combining a machine learning algorithm and DBSI metrics, to accurately identify and classify various histopathological components of GBM.

Materials and Methods

Study Design

The study was approved by institutional review board. Informed consent was obtained from all participants. We recruited 16 GBM patients between June 2015 and November 2018 to participate in this study. We applied *in vivo* Gd-enhanced T1WI, FLAIR, and DBSI on GBM patients (n=3) to obtain multi-metric maps to examine the relative spatial distribution of DBSI metrics among Gd-enhanced, non Gd-enhanced, and hyperintense FLAIR regions. To determine underlying microstructural changes in GBM pathologies, we collected 19 surgically-resected specimens from 13 neurosurgical patients. A more detailed description of experimental procedures including sample preparation, MRI data acquisition, image registration and processing, and data analysis can be found in Supplementary Materials and Methods.

Ex Vivo MRI of Surgical Resection Tumor Specimens

Specimens were formalin-fixed at time of collection and then agarose-gel-embedded before being examined using a 4.7-T Agilent MR scanner (Agilent Technologies, Santa Clara, CA) with a home-made circular surface coil (1.5-cm diameter). A multi-echo spin-echo diffusion-weighted sequence with 99 diffusion-encoding directions with maximum b-values at 3000 s/mm^2 was employed to acquire DW images with a 0.25×0.25 mm^2 in-plane resolution, and 0.5-mm thickness.

Total acquisition time was approximately 4 hours. MR images were zero-filled to 0.125×0.125 mm^2 in-plane resolution for DBSI and DTI analyses.

Cellularity Quantified in H&E and GFAP

We developed a procedure involving down-sampling histological images and co-registering MRI with histological images to enable the voxel-wise correlation between DBSI-restricted diffusion fraction and tumor cellularity. Detailed analysis was performed as described in Supplementary Materials and Methods. Briefly, specimens were sectioned and stained after *ex vivo* MRI to acquire H&E and GFAP images. High resolution histology images were down-sampled to match DBSI/DTI resolution (125×125 μm^2) to enable direct comparison between DBSI/DTI and histological images. Each down-sampled image voxel contained 272×272 original image pixels. A two-dimensional (2D) thin-plate-spline (TPS) co-registration method was adopted using 50 manually-picked landmarks.

***In Vivo* MRI of Human Subjects**

A 3-T Siemens TIM Trio (Erlanger, Germany) with a 32-channel head coil was used for all *in vivo* images. MRI data were acquired using a 99-direction diffusion-weighting encoding scheme with maximum b-value of 1500 s/mm^2 at 2×2×2 mm^3 resolution in axial plane covering whole brain. Acquisition time for DBSI per case was 10 minutes.

Recapitulating Neuropathological Analysis of GBM

The gold standard for detecting tumor is histopathology, reliant on a pathologist's recognition of structural features in tissue specimens and thus requires a surgical procedure with inherent risk. To

develop a non-invasive tool that can recapitulate histopathological specificity of tumor induced structural changes, we have developed a novel DHI approach, combining DBSI-derived structural metrics with machine learning, to detect, differentiate, and quantify areas of high tumor cellularity, tumor necrosis, and tumor-infiltrated brain in GBM.

DBSI models brain tumor diffusion-weighted MRI signals as a linear combination of discrete multiple anisotropic diffusion tensors and a spectrum of isotropic diffusion tensors:

$$\frac{S_k}{S_0} = \sum_{i=1}^{N_{Aniso}} f_i \, e^{-\left|\vec{b_k}\right|\lambda_{\perp i}} e^{-\left|\vec{b_k}\right|(\lambda_{\parallel i}-\lambda_{\perp i})\cos^2\phi_{ik}} + \int_a^b f(D) e^{-\left|\vec{b_k}\right|D} dD \; (k = 1,2,3,\dots). \qquad [1]$$

Here b_k is the k^{th} diffusion gradient; S_k/S_0 is the acquired diffusion-weighted signal at direction of b_k normalized to non-diffusion-weighted signal; N_{Aniso} is number of anisotropic tensors to be determined; ϕ_{ik} is the angle between diffusion gradient b_k and principal direction of the i^{th} anisotropic tensor; $\left|\vec{b_k}\right|$ is b-value of the k^{th} diffusion gradient; $\lambda_{||i}$ and $\lambda_{\perp i}$ are axial and radial diffusivity of the i^{th} anisotropic tensor under the assumption of cylindrical symmetry; f_i is signal-intensity-fraction of the i^{th} anisotropic tensor; *a, b* are low and high diffusivity limits of isotropic diffusion spectrum; *f(D)* is signal-intensity-fraction at isotropic diffusivity *D*.

We preliminarily examined diffusion-weighted MRI signal patterns from different histopathological structures to determine the associated DBSI-metric profiles. Based on the training set of 21 specimen sections, the following isotropic-diffusion profiles were established: highly-restricted isotropic diffusion, associated with lymphocytes (summation of $f(D)$ at $0 \leq D \leq 0.2$ $\mu m^2/ms$); restricted-isotropic diffusion, associated with GBM tumor cells (summation of $f(D)$ at $0.2 < D \leq 0.8$ $\mu m^2/ms$); and hindered-isotropic diffusion, associated with tumor necrosis (summation

of $f(D)$ at 0.8<D≤2 μm^2/ms). To extend these *ex vivo* diffusion MRI metric profiles to *in vivo* human subjects, we employed the following profiles: highly restricted diffusion fraction, summation of $f(D)$ at 0≤D≤0.2 μm^2/ms; restricted isotropic diffusion, summation of $f(D)$ at 0.2<D≤1.5 μm^2/ms, and hindered isotropic diffusion, summation of $f(D)$ at 1.5<D≤2.5 μm^2/ms.

Eq. [1] provides a simple tensor expression to visualize morphological features resulting from tumor formation and non-tumor entities appearing indistinct to tumor by conventional MRI. For example, in an image voxel where normal white matter tracts and gray matter is coexisting with the presence of tumor cells. The tensor function of anisotropic and isotropic tensors will not change comparing with the normal tissues with the exception of changes resulting from the presence of tumor cells. If tumor cells also introduce vasogenic edema within this image voxel, extra tensor function will manifest as restricted (representing tumor cells) and hindered (representing vasogenic edema) isotropic tensors. The different tensor expressions of individual image voxels thus bear morphological signatures of underlying pathology. In the case where tumor cells happen to also damage white matter tracts resulting, say, axonal injury and demyelination. The isotropic tensors within this image voxel will remain the same but now anisotropic diffusion tensor will exhibit decreased axial diffusivity and increased radial diffusivity. It is the sensitivity of diffusion-weighted MRI signal to the microstructural changes in the scale up to 10 μm range (depending how one adjusts diffusion-weighting condition) that allows DBSI to more precisely reflect morphological changes resulting from tumor presence or other pathological conditions. By taking the advantage of this feature of DBSI as the input of machine learning algorithms, we created DHI to recapitulate histopathological analysis using MRI.

Statistical Analysis

We used Spearman's rank correlation to measure strengths of monotonically increasing or decreasing associations. Statistically significant results were determined at a predetermined alpha level of 0.05.

To construct a machine learning classifier for histopathological prediction, support vector machine (SVM) with polynomial kernel algorithm was adopted. We performed a linear co-registration between MRI and corresponding neuropathologist-classified H&E images to label each imaging voxel with the gold standard of pathology. Total 21 specimen sections from 19 brain tumor specimens (6605 image voxels) were analyzed to determine DBSI and DTI metrics profiles of each voxel. Imaging voxels from four specimen sections were used for cross-validation testing. The remaining voxels from other sections were randomly split into training and validation datasets with 1:1 ratio. Total 1000 distinct training-prediction group pairings were run to prevent selection bias. Mean values and 95% confidence intervals were calculated.

Confusion matrices were calculated to illustrate the specific examples of tumor pathologies where predictions were discordant with pathologist-identified pathologies. We evaluated overall accuracy of classifying testing voxels as well as true positive rate, true negative rate and positive predictive value of the model prediction. Receiver operating characteristics (ROC) and precision-recall (PR) curves were calculated using a one-versus-rest strategy to assess model discrimination for each tumor pathology. Area under curves (AUC) and F_1-scores were calculated to compare the relative performance of DHI to pathologist-identified pathologies.

Results

Patient Information

Among the sixteen patients, eleven were male. The mean age at diagnosis was 61.1±14.2 years. Pathological analysis of tumor specimens confirmed isocitrate dehydrogenase (*IDH)*-wildtype GBM in all 16 patients (Table S1).

DBSI Metrics Are Not Unique to Gd-Enhanced, Non-Enhaned T1W or Hyperintense FLAIR Tumor Regions in Patients

We performed clinical MRI and DBSI on three GBM patients. Representative Gd-enhanced T1W, FLAIR, T2W, DBSI, and ADC images were obtained from a 79-year-old male patient with a right temporal GBM (Fig. 1A). We outlined Gd-enhanced and non-enhanced T1W regions to compare the underlying DBSI metrics in these regions, overlaid on MPRAGE-T1W images (Fig. 1A). Based on our DBSI modeling and previous studies, we would predict that DBSI metrics of restricted fraction, hindered fraction, and anisotropic fraction, represent high tumor cellularity, necrosis, and white matter tracts, respectively. Strikingly, DBSI metrics of restricted fraction (red), hindered fraction (blue), and anisotropic fraction (green) were entangled in both Gd-enhancing and non-enhancing regions (Fig. 1A, DBSI). Specifically, hyperintensity of restricted fraction were widespreaded in Gd non-enhancing region where histology is typically considered to be necrosis, indicating the potential high tumor cellularity in this region that could significantly challenge the current clinical standard.

To determine if specific DBSI structural metrics are enriched in particular clinical MRI sequences, we generated histograms of DBSI-metrics from Gd-enhancing, non-enhancing, and FLAIR hyperintense lesions from all three patients (Fig. 1B). The common feature among the three GBM cases was the consistent presence of all three DBSI structural metrics in all clinical MRI-defined lesions. Qualitatively, the pattern of DBSI metric distributions did not appear to be unique

for Gd-enhancing, non-enhancing, and FLAIR hyperintense regions of GBM tumors, suggesting that these clinical MRI-defined regions harbor mixed pathologies.

Tumor Cellularity Correlated with DBSI-Restricted Fraction, but Not ADC, in *Ex Vivo* GBM Specimens

As shown above (Fig. 1), *in vivo* DBSI restricted, hindered, and anisotropic fractions were highly overlapping in MR-lesions of GBM. To definitively determine relationships between DBSI metrics and GBM pathologies, we examined *ex vivo* DBSI metrics in histologically-identified regions of high tumor cellularity, tumor necrosis, and tumor infiltration in 19 surgically-resected specimens. We performed a thin-plate-spline co-registration on specimens correlating diffusion-weighted images with H&E and glial fibrillary acidic protein (GFAP) cellularity maps (Fig. 2A/B) to allow voxel-to-voxel correlation of histology (H&E and GFAP positive area ratio maps) with ADC, and DBSI-restricted fraction maps (Fig. 2C). We randomly selected fifty voxels from down-sampled H&E images (Fig. 2A, red squares) and mapped them to the co-registered GFAP, MRI-metric maps for voxel-based correlation. Out of twenty specimens, fifteen underwent MRI-H&E and nine underwent MRI-GFAP correlation analyses. The rest were excluded due to unmatched sectioning planes.

Spearman's rank correlation for selected voxels from all specimens (Fig. 2C) was used to assess the general performance of imaging biomarkers for cellularity in tumor samples. Restricted fraction correlated with H&E ($r=0.53$, $p<0.0001$) and GFAP positive areas ($r=0.66$, $p<0.0001$). In contrast, ADC failed to correlate with H&E ($r=-0.078$, $p=-0.055$) or GFAP ($r=0.04$, $p=0.28$).

Qualitative Comparison of DBSI Metrics with GBM Pathologies

To definitively determine relationships between DBSI metrics and GBM pathologies, we examined *ex vivo* DBSI metrics in histologically-identified regions of high tumor cellularity, tumor necrosis, and tumor infiltration in 19 surgically-resected specimens. A representative tumor specimen (10.1×8.7 mm^2) from a 77-year-old female patient demonstrates the relationship between DBSI metrics and tumor pathologies (Fig. 3). Hyperintense DWI (*i.e.* hypointense ADC) defined voxels did not correspond to H&E measures of cellularity (Fig. 2 and 3A/B). By co-registering DWI with histological images, representative regions from high tumor cellularity (red square), tumor infiltration (green square), and tumor necrosis (blue square) were selected and enlarged (Fig. 3B). High tumor cellularity areas exhibited peaks at highly-restricted and restricted diffusion regions of DBSI-isotropic diffusion spectrum; infiltrated white matter exhibited peaks at the same locations as high cellularity with varying intensities; and tumor necrosis exhibited highly-restricted and hindered diffusion peaks (Fig. 3C). The distribution of DBSI restricted, hindered, and anisotropic fraction maps were generated according to empirically-determined thresholds from the analysis of all specimens with matched H&E and DBSI. Although DBSI metrics were overlapping in these pathologies (Fig. 1A/B and 3C), DBSI restricted and hindered fraction maps qualitatively resembled areas of high tumor cellularity and tumor necrosis, respectively, as identified by a neuropathologist (Fig. 3D).

Accurate Prediction of Pathological Features in GBM Using Diffusion Histology Imaging

Through image co-registration, MRI voxels corresponding to pathologically-verified areas of high tumor cellularity, tumor necrosis, and tumor infiltration were identified. Image voxel values of DTI (Fig. 4A) and DBSI (Fig. 4B) metrics are presented to demonstrate the distinctions and similarities among these identified tumor pathologies. A multi-parametric examination based on

restricted fraction, hindered fraction, and isotropic fraction separated the three pathologically distinct entities (Fig. 4C), suggesting analysis based on multiple DBSI metrics could potentially better distinguish among these pathologies rather than single DBSI metrics alone.

We thus developed DHI incorporating a supervised SVM algorithm with modified-DBSI (incorporating a distinction between inflammation and tumors) derived structural metrics as classifiers to construct predictive models to distinguish among different tumor histopathology. We trained and validated the predictive model on image voxels from 17 of the 21 GBM specimen sections. The established model was applied to image voxels from four remaining GBM specimen sections to predict distributions of high tumor cellularity (Fig. 4D, red), tumor necrosis (Fig. 4D, blue) and tumor infiltration (Fig. 4D, green) with 96.2% overall accuracy (n=1963). DHI correctly predicted 97.2%, 96.6% and 91.8% of the image voxels as high tumor cellularity, tumor necrosis, and tumor infiltration, respectively.

A comparison between DHI and DTI-SVM was performed using confusion matrices. The DHI (Fig. 4E) approach demonstrated better prediction accuracy for tumor pathologies compared to DTI-SVM (Fig. 4F). We also performed ROC and precision-recall curves analyses for each tumor pathological feature (Fig. 4E, F). DHI indicated greater ROC and precision-recall AUC values for all the pathological features than DTI-SVM.

Pathological Validation of DHI

From four DHI test specimens, we randomly selected four DWI voxels from each specimen (Fig. 6A–D) and use corresponding histology as validation. This was achieved by tracking each voxel back to the co-registered down-sampled histological images to compare DHI-predicted

pathologies with gold standards. We observed high predictive performance of DHI on individual specimens.

DHI predicted 94.3% of high tumor cellularity areas (Fig. 6A, red), 97.3% of necrotic areas (Fig. 6A, blue) and 82.1% of tumor infiltration areas (Fig. 6A, green) in a 77-year-old patient specimen (B122). Indeed, corresponding H&E image tiles (i.e., voxels of down-sampled histology images) verified the randomly-selected DHI predictions of high tumor cellularity (Fig. 6A: a, b), tumor infiltration (Fig. 6A: c), and tumor necrosis (Fig. 6A: d). The second test specimen from a 54-year-old patient (B95) exhibited 98.0% accuracy of DHI predictions of high tumor cellularity voxels (Fig. 6B, red) and 93.3% true prediction rates of tumor necrosis (Fig. 6B, blue) as validated by corresponding H&E image tiles (high tumor cellularity (Fig 6B: a, b) and tumor necrosis (Fig 6B: c, d). The third specimen from a 47-year-old female patient (B128) was also assessed, demonstrating that DHI predicted voxels of high tumor cellularity was 99.0% accurate (Fig. 6C: a, b, c, d). In the fourth test specimen from a 57-year-old patient (B94), DHI correctly predicted 100% of tumor infiltration voxels (Fig. 6D). Corresponding H&E image tiles all indicated tumor infiltration patterns.

Comparing DTI-SVM and DHI Performance on Predicting Tumor Pathologies

We ran 1000 different train-test-split pairings to avoid possible selection bias resulting from the use of specific test subjects. The results were summarized in Table 1. The mean accuracy of DHI was 89.6%, compared to 76.7% of DTI-SVM. Mean true prediction rates of DHI for high tumor cellularity, tumor necrosis, and tumor infiltration were 87.5%, 89.0% and 93.4%, respectively. By contrast, mean true prediction rates of DTI-SVM were 76.7%, 62.3% and 97.9%, respectively. Additionally, DHI showed much better overall precision-recall performances, with mean F_1 scores

of DHI as 0.917, 0.823 and 0.876 for three tumor pathologies. We further performed ROC analyses to test how well our classifiers differentiate between pairwise tumor pathologies (e.g., infiltration vs. non-infiltration). The ROC analysis results revealed that DHI had great performance on distinguishing these three tumor pathologies, with mean AUC values of 0.975, 0.989 and 0.951 for high tumor cellularity, tumor necrosis, and tumor infiltration, respectively. In contrast, DTI-SVM did not perform as well as DHI (Table 1).

Discussion

The standard of care for GBM involves surgical resection, followed by radiotherapy with concurrent and adjuvant chemotherapy. Histological assessment of tumor cellularity, necrosis, and infiltration plays a vital role in the clinical decision-making for the management of GBM patients. The current gold standard of pathological examination following stereotactic biopsy or surgical resection[16] carries potential risks.[17] On some occasions, inconclusive pathological findings may result from inadequate sampling that may necessitate repeat procedures.[18] Thus, noninvasive neuroimaging approaches to facilitate diagnosis or to guide biopsies and surgical planning are needed to improve GBM patient care.

Through voxel-wise comparisons with histological images, we demonstrated that DBSI-derived restricted-isotropic-diffusion fraction, hindered-isotropic-diffusion fraction, and anisotropic-diffusion-fraction closely correlate with cellularity, tumor necrosis, and white matter tracts, respectively. However, these metrics alone were not sufficient to clearly distinguish high tumor cellularity, tumor necrosis, or tumor infiltration (Figs. 1, 3 and 4). We thus developed DHI, incorporating a SVM predictive model using DBSI metrics as the classifiers, to successfully

predict high tumor cellularity, tumor necrosis, and tumor infiltration against the gold standard of histology with high accuracy (Figs. 4-6).

Various neuroimaging techniques have been tested to assess the treatment response of brain tumors in clinical practice. Among the wide range of available neuroimaging modalities, contrast-enhanced T1WI is currently the method of choice for brain tumor diagnosis. Unfortunately, Gd-enhanced T1WI lacks specificity because it merely reflects a disrupted blood-brain barrier.[19] Chemotherapy, radiation, and newer clinical trial treatments such as immunotherapies produce neuroimaging lesions that mimic tumor progression or recurrence, further confounding clinical decision making.[20] These and other shortcomings of current clinical MRI sequences suggest limitations of the MacDonald criteria[4] and the Response Assessment in Neuro-Oncology (RANO) updated response assessment criteria[3,21] in monitoring tumor burden. Therefore, there is an urgent need to develop imaging modalities that can non-invasively detect and characterize the histological features of post-treatment GBM for appropriate treatment planning.

Advanced MRI methods, such as perfusion-weighted imaging with and without contrast[22,23] and chemical exchange saturation transfer (CEST) imaging,[24] and positron emission tomography (PET) with amino acid tracers, including [11C]-methyl-L-methionine (MET),[25] O-(2-[18F]-fluoroethyl)-L-tyrosine (FET),[26] 3,4-dihydroxy-6-[18F]-fluoro-L-phenylalanine (FDOPA),[27] also provide complementary diagnostic information in GBM detection. In addition, stimulated Raman scattering microscopy,[28] optical coherence tomography,[29] and mass spectroscopy[30] have also been developed to improve glioma diagnosis. However, most of these techniques do not have the capability of quantifying individual pathological components in a non-invasive manner.

To address limitations of conventional MRI, diffusion-weighted MRI-derived ADC has been one of the most widely researched tools for the evaluation of tumor cellularity and grade.[10] Although increased tumor cellularity has been associated with decreased ADC, the expression of aquaporin in high-grade glioma,[31] vasogenic edema,[32] and necrosis[33] may obviate the interpretation of expected diffusion restriction caused by high cellularity. Indeed, in our tested tumor specimens, ADC did not correlate with cellularity while the DBSI-derived restricted fraction significantly correlated with both H&E- and GFAP staining-based cellularity measures (Fig. 2). One observation in the present study contradicting the widely-accepted role of ADC in tumor cellularity is the significantly restricted diffusion observed in white matter tracts (Fig. 3), where the disrupted fiber network greatly increased diffusion restriction. Thus, our results further support that ADC alone cannot be considered a reliable tumor biomarker.

Through histological validation, we demonstrated DHI accurately detects and quantifies high tumor cellularity, tumor necrosis, and tumor infiltration. The newly-developed DHI framework accurately predicted key features of GBM microenvironment that eluded other neuroimaging technologies. Given the lack of specificity of clinical MRI in identifying tumor burden, DHI has the potential to aid in the non-invasive determination of tumor recurrence vs. treatment response. In addition, pre-operative DHI may help to guide biopsies and improve extent of resection.

References

1. Ostrom QT, Gittleman H, Truitt G, Boscia A, Kruchko C, Barnholtz-Sloan JS. CBTRUS Statistical Report: Primary Brain and Other Central Nervous System Tumors Diagnosed in the United States in 2011-2015. *Neuro-oncology.* 2018; 20(suppl_4):iv1-iv86.

2. Louis DN. Molecular pathology of malignant gliomas. *Annual review of pathology.* 2006; 1:97-117.

3. Wen PY, Macdonald DR, Reardon DA, et al. Updated response assessment criteria for high-grade gliomas: response assessment in neuro-oncology working group. *Journal of clinical oncology : official journal of the American Society of Clinical Oncology.* 2010; 28(11):1963-1972.

4. Macdonald DR, Cascino TL, Schold SC, Jr., Cairncross JG. Response criteria for phase II studies of supratentorial malignant glioma. *Journal of clinical oncology : official journal of the American Society of Clinical Oncology.* 1990; 8(7):1277-1280.

5. Chang SM, Parney IF, Huang W, et al. Patterns of care for adults with newly diagnosed malignant glioma. *Jama.* 2005; 293(5):557-564.

6. Brem SS, Bierman PJ, Brem H, et al. Central nervous system cancers. *Journal of the National Comprehensive Cancer Network : JNCCN.* 2011; 9(4):352-400.

7. Henegar MM, Moran CJ, Silbergeld DL. Early postoperative magnetic resonance imaging following nonneoplastic cortical resection. *Journal of neurosurgery.* 1996; 84(2):174-179.

8. Kumar AJ, Leeds NE, Fuller GN, et al. Malignant gliomas: MR imaging spectrum of radiation therapy- and chemotherapy-induced necrosis of the brain after treatment. *Radiology.* 2000; 217(2):377-384.

9. Ulmer S, Braga TA, Barker FG, 2nd, Lev MH, Gonzalez RG, Henson JW. Clinical and radiographic features of peritumoral infarction following resection of glioblastoma. *Neurology.* 2006; 67(9):1668-1670.

10. Malayeri AA, El Khouli RH, Zaheer A, et al. Principles and applications of diffusion-weighted imaging in cancer detection, staging, and treatment follow-up. *Radiographics : a review publication of the Radiological Society of North America, Inc.* 2011; 31(6):1773-1791.

11. Kang Y, Choi SH, Kim YJ, et al. Gliomas: Histogram analysis of apparent diffusion coefficient maps with standard- or high-b-value diffusion-weighted MR imaging--correlation with tumor grade. *Radiology.* 2011; 261(3):882-890.

12. Gerstner ER, Chen PJ, Wen PY, Jain RK, Batchelor TT, Sorensen G. Infiltrative patterns of glioblastoma spread detected via diffusion MRI after treatment with cediranib. *Neuro-oncology.* 2010; 12(5):466-472.

13. Wang Y, Sun P, Wang Q, et al. Differentiation and quantification of inflammation, demyelination and axon injury or loss in multiple sclerosis. *Brain : a journal of neurology.* 2015; 138(Pt 5):1223-1238.

14. Murphy RK, Sun P, Xu J, et al. Magnetic Resonance Imaging Biomarker of Axon Loss Reflects Cervical Spondylotic Myelopathy Severity. *Spine.* 2016; 41(9):751-756.

15. Zhan J, Lin TH, Libbey JE, et al. Diffusion Basis Spectrum and Diffusion Tensor Imaging Detect Hippocampal Inflammation and Dendritic Injury in a Virus-Induced Mouse Model of Epilepsy. *Frontiers in neuroscience.* 2018; 12.

16. McGirt MJ, Villavicencio AT, Bulsara KR, Friedman AH. MRI-guided stereotactic biopsy in the diagnosis of glioma: comparison of biopsy and surgical resection specimen. *Surgical neurology.* 2003; 59(4):277-281; discussion 281-272.

17. Apuzzo ML, Chandrasoma PT, Cohen D, Zee CS, Zelman V. Computed imaging stereotaxy: experience and perspective related to 500 procedures applied to brain masses. *Neurosurgery.* 1987; 20(6):930-937.

18. Air EL, Warnick RE, McPherson CM. Management strategies after nondiagnostic results with frameless stereotactic needle biopsy: Retrospective review of 28 patients. *Surgical neurology international.* 2012; 3(Suppl 4):S315-319.

19. Smirniotopoulos JG, Murphy FM, Rushing EJ, Rees JH, Schroeder JW. Patterns of contrast enhancement in the brain and meninges. *Radiographics : a review publication of the Radiological Society of North America, Inc.* 2007; 27(2):525-551.

20. Villanueva-Meyer JE, Mabray MC, Cha S. Current Clinical Brain Tumor Imaging. *Neurosurgery.* 2017; 81(3):397-415.

21. Vogelbaum MA, Jost S, Aghi MK, et al. Application of novel response/progression measures for surgically delivered therapies for gliomas: Response Assessment in Neuro-Oncology (RANO) Working Group. *Neurosurgery.* 2012; 70(1):234-243; discussion 243-234.

22. Morana G, Piccardo A, Tortora D, et al. Grading and outcome prediction of pediatric diffuse astrocytic tumors with diffusion and arterial spin labeling perfusion MRI in comparison with 18F-DOPA PET. *Eur J Nucl Med Mol Imaging.* 2017; 44(12):2084-2093.

23. Falk A, Fahlstrom M, Rostrup E, et al. Discrimination between glioma grades II and III in suspected low-grade gliomas using dynamic contrast-enhanced and dynamic susceptibility

contrast perfusion MR imaging: a histogram analysis approach. *Neuroradiology.* 2014; 56(12):1031-1038.

24. Zhou JY, Tryggestad E, Wen ZB, et al. Differentiation between glioma and radiation necrosis using molecular magnetic resonance imaging of endogenous proteins and peptides. *Nat Med.* 2011; 17(1):130-U308.

25. Delgado AF, Delgado AF. Discrimination between primary low-grade and high-grade glioma with C-11-methionine PET: a bivariate diagnostic test accuracy meta-analysis. *Brit J Radiol.* 2018; 91(1082).

26. Pauleit D, Floeth F, Hamacher K, et al. O-(2-[F-18]fluoroethyl)-L-tyrosine PET combined with MRI improves the diagnostic assessment of cerebral gliomas. *Brain : a journal of neurology.* 2005; 128:678-687.

27. Isal S, Gauchotte G, Rech F, et al. A high F-18-FDOPA uptake is associated with a slow growth rate in diffuse Grade II-III gliomas. *Brit J Radiol.* 2018; 91(1084).

28. Ji M, Lewis S, Camelo-Piragua S, et al. Detection of human brain tumor infiltration with quantitative stimulated Raman scattering microscopy. *Science translational medicine.* 2015; 7(309):309ra163.

29. Kut C, Chaichana KL, Xi JF, et al. Detection of human brain cancer infiltration ex vivo and in vivo using quantitative optical coherence tomography. *Science translational medicine.* 2015; 7(292).

30. Eberlin LS, Norton I, Orringer D, et al. Ambient mass spectrometry for the intraoperative molecular diagnosis of human brain tumors. *Proceedings of the National Academy of Sciences of the United States of America.* 2013; 110(5):1611-1616.

31. McCoy E, Sontheimer H. Expression and function of water channels (aquaporins) in migrating malignant astrocytes. *Glia.* 2007; 55(10):1034-1043.

32. Castillo M, Smith JK, Kwock L, Wilber K. Apparent diffusion coefficients in the evaluation of high-grade cerebral gliomas. *AJNR. American journal of neuroradiology.* 2001; 22(1):60-64.

33. Verma N, Cowperthwaite MC, Burnett MG, Markey MK. Differentiating tumor recurrence from treatment necrosis: a review of neuro-oncologic imaging strategies. *Neuro Oncol.* 2013; 15(5):515-534.

Figure Legends

Fig. 1. Gd-enhanced T1WI or hyper-intense FLAIR failed to reflect the morphological complexity underlying GBM. We segmented hyper- and hypo-intense Gd-T1W lesions, and hyper-intense FLAIR lesion (A) to quantitatively analyze DBSI metrics (B) from three patients. Representative MR images of GBM at the right temporal lobe were obtained from a 79-year-old male patient (A). Both Gd-enhanced and non Gd-enhanced regions exhibit various extents of restricted diffusion (red), hindered diffusion (blue), and anisotropic diffusion (green), suggesting the lack of pathological or structural specificity of the widely used Gd-enhanced T1W and hyper-intense FLAIR lesion. A more quantitative analysis is assessed by the histogram of DBSI metrics from these three lesions (B; x-axis=fraction of DBSI metric; y-axis=number of occurrence). Contrary to widely accepted notion that Gd-enhanced T1WI lesion is primarily associated with tumor cellularity, we observed the elevated putative DBSI cellularity marker (restricted fraction; scale 0-0.6) in both Gd-enhanced and non Gd-enhanced regions. Putative DBSI vasogenic edema or tissue loss (hindered fraction; scale 0-1.0) is also seen in both regions. DBSI anisotropic diffusion fraction (reflecting the extent of white matter tracts; scale 0-1.0) is also present in both Gd-enhanced and non Gd-enhanced regions. As seen in these three subjects (B, subject 3 does not have a non Gd-enhanced lesion), the three DBSI metrics are present in all Gd-enhanced, non Gd-enhanced and FLAIR hyperintense lesions, further supporting the insufficiency of these commonly employed imaging markers.

Fig. 2. MRI-Histology co-registration and quantification. (A) Quantitative cellularity maps were calculated from high resolution H&E images. High-resolution H&E images were down-

sampled to match MRI resolution (125×125 μm^2). Individual tiles of MRI voxels containing 272×272 high-resolution H&E image pixels were extracted. Fractions of positively-stained area of individual image tiles were computed from ratios between positively-stained areas and total pixel areas and color-coded then stitched back to construct the quantitative cellularity map. **(B)** We performed co-registration of DWI and H&E images to allow voxel-to-voxel correlation of histology with ADC, DBSI-isotropic ADC, and DBSI-restricted fraction. Around fifty Landmarks were manually placed along the perimeter of diffusion-weighted images and down-sampled histology images for co-registration. The transformation function of thin-plate-spline co-registration was applied to warp MR images to match histology images. Fifty image voxels were randomly selected from each down-sampled H&E image and applied to all co-registered maps for correlation and quantitative analysis. **(C)** Regression analysis of DTI-ADC vs. H&E and DTI-ADC vs. GFAP suggested weak correlations (r=-0.078, -0.055 and p=0.04, 0.28, respectively). DBSI isotropic-ADC showed the expected negative correlation with H&E-cellularity (r=-0.16, p=0.00004) but did not correlate with GFAP-cellularity (r=0.07, p=0.13). DBSI-restricted fraction displayed statistically significantly high correlation with H&E- and GFAP-cellularity (r=0.53, 0.66, respectively; $p<0.0001$).

Fig. 3. Association between DBSI-metrics and neuropathologist-identified tumor pathology. A surgically-resected specimen from a 77-year-old female GBM patient was analyzed via T2WI and DWI (A). Neuropathologist identified high tumor cellularity, tumor infiltration, and tumor necrosis regions in H&E and GFAP staining slides and digitized images (B). According to the widely-accepted notion, a hyper-intense DWI (red arrow), i.e., hypo-intense ADC (red arrow), region is suggestive of increased tumor cellularity. However, it does not match neuropathologist-

identified pathology featuring white matter tracts with tumor infiltration based on histology staining (B), consistent with figure 2 findings. From the co-registered MRI-histology images, high tumor cellularity, tumor infiltration, and tumor necrosis regions were matched with DBSI-metrics. High tumor cellularity signal (red) exhibits peaks at highly-restricted and restricted diffusion regions; infiltrated white matter signal (green) exhibits peaks at the same locations as high cellularity with varying intensities; and tumor necrosis signal (blue) exhibits highly-restricted and hindered diffusion regions (C). Based on these distributions, we generated DBSI highly-restricted, restricted, and hindered isotropic-diffusion signal fraction maps (D). These maps reveal that highly-restricted fraction is high in tumor infiltration and high tumor cellularity regions; restricted fraction is highly associated with high tumor cellularity regions (consistent with findings of figure 2); and hindered diffusion fraction is highly correlated with H&E tumor necrosis regions. The intensity gradient on restricted fraction map reflects tumor cellularity change.

Fig. 4. Classifying high tumor cellularity, tumor necrosis and tumor infiltration in resected GBM specimens. The structural metrics derived from DBSI (A) and DTI (B) were obtained in neuropathologist-identified high tumor cellularity (red), tumor necrosis (blue), and tumor infiltration (green) regions through MRI-histology co-registration. Overlapping profiles of DTI/DBSI structural metrics are common within individual tumor pathology. Thus, it is difficult to distinguish tumor pathologies by thresholding single diffusion metrics values. Representative neuropathologist-identified histology-image voxel values of DBSI restricted, hindered, and anisotropic fractions reveal that the three tumor pathologies can be resolved by combining the three DBSI metrics (C). Representative histology images corresponding to selected DBSI image voxels were presented. For this independent dataset (n=1963), DHI predicted voxels showed great

match with histology, affording a 96.2% overall accuracy in predicting high tumor cellularity, tumor necrosis and tumor infiltration (D). Confusion matrices reveal DHI (E) is more accurate than DTI-SVM (F) in predicting high tumor cellularity, tumor necrosis and tumor infiltration. Additionally, DHI showed greater AUC values than DTI-SVM on both ROC and precision-recall curves.

Fig. 5. Histology validation of DHI determined tumor pathologies in the four test specimens. In a 77-year-old female GBM patient (B122) specimen, DHI correctly predicts high tumor cellularity (A, red), tumor necrosis (A, blue) and tumor infiltration (A, green) with 94.3%, 97.3% and 82.1%, respectively. Corresponding H&E image tiles verify the randomly-selected DHI-determined high tumor cellularity (A: a, b), infiltration (A: c) and necrosis (A: d). The second test specimen from a 54-year-old GBM patient (B95) exhibits a 98.0% and 93.3% true prediction rate of DHI-determined high tumor cellularity and necrosis voxels, respectively, validated by corresponding H&E image tiles: high tumor cellularity (B: a, b) and tumor necrosis (B: c, d). The third specimen from a 47-year-old female GBM patient (B128) was also assessed to reveal that DHI-determined high tumor cellularity is 99.0% accurate, as validated by the H&E tiles (C: a, b, c, d). In the fourth test specimen from a 57-year-old GBM patient (B94), DHI correctly predicted 100% of the tumor infiltration voxels (D). All the four selected voxels from co-registered H&E (D: a, b, c, d) indicated tumor infiltration pattern.

Figure 1

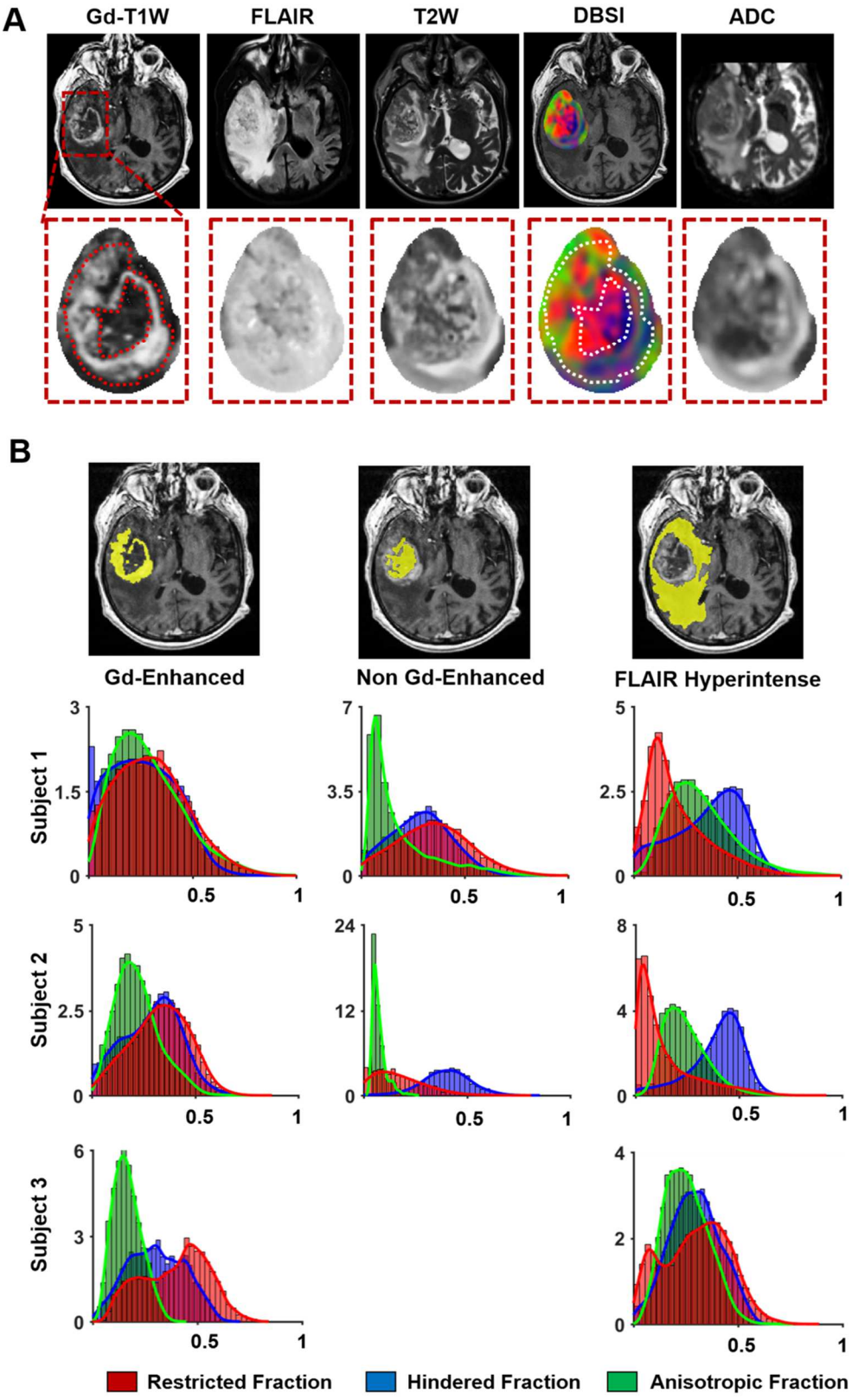

Figure 2

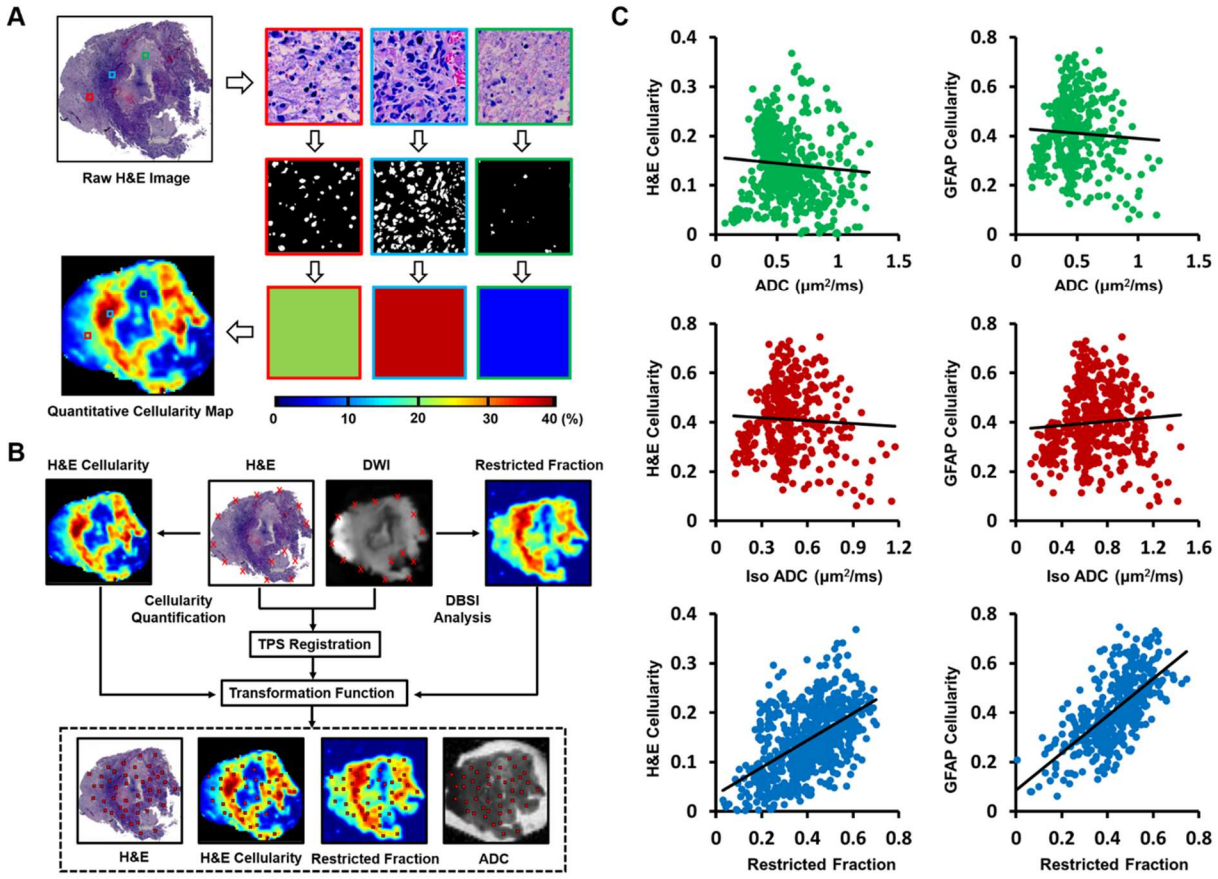

Figure 3

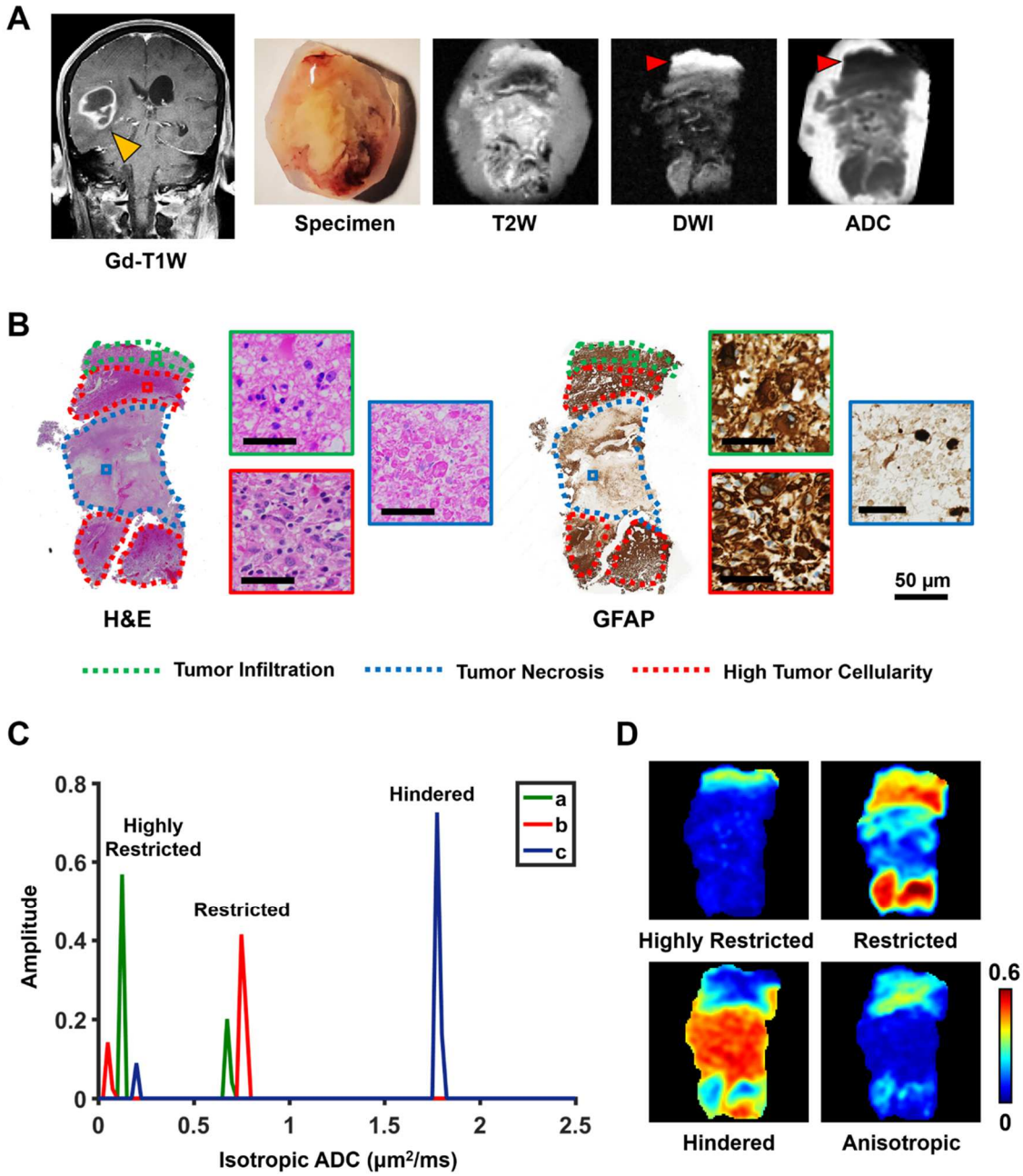

Figure 4

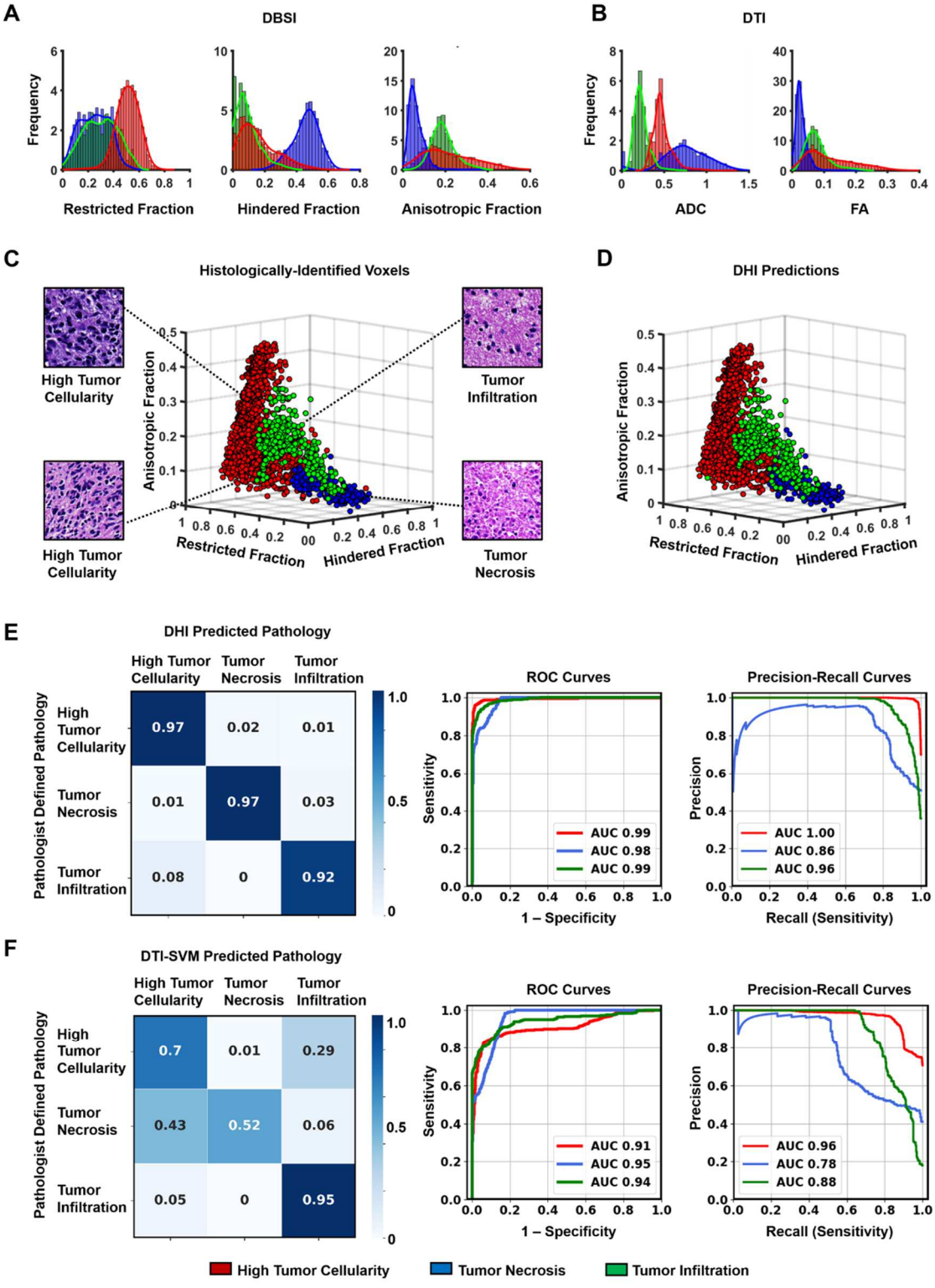

Figure 5

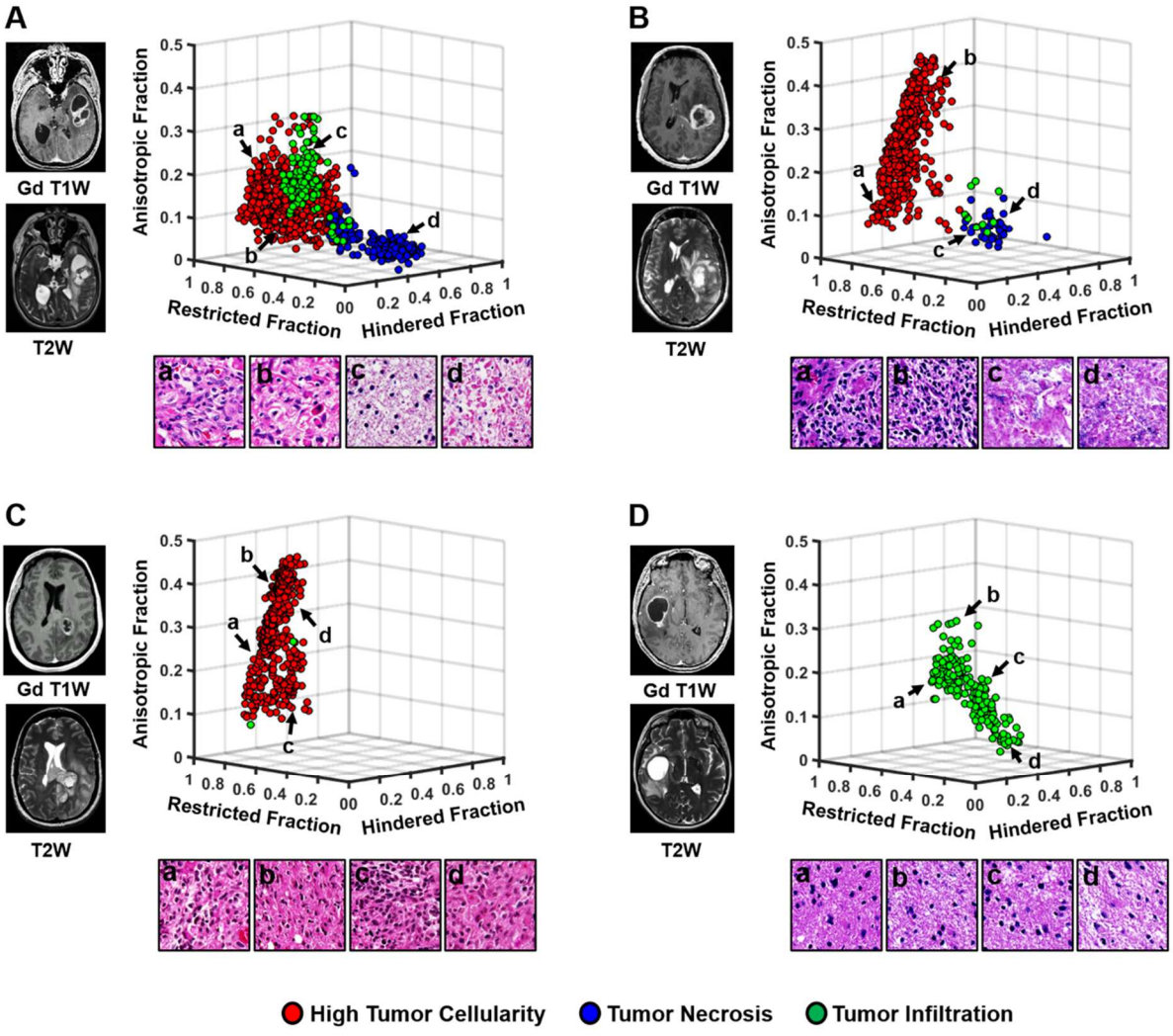

Table 1. Comparing Diagnostic Performances of DHI and DTI-SVM on Predicting Tumor Pathologies.

Predictive Model	Pathology	TPR (%)	TNR (%)	PPV (%)	F_1 Score	AUC
DHI	High Tumor Cellularity	87.5 (86.7-88.3)	95.3 (94.9-95.8)	97.0 (96.7-97.3)	0.917 (0.911-0.923)	0.975 (0.973-0.976)
	Tumor Necrosis	89.0 (88.3-89.8)	92.9 (92.5-93.4)	78.2 (76.8-79.6)	0.823 (0.814-0.833)	0.951 (0.947-0.955)
	Tumor Infiltration	93.4 (92.7-94.0)	95.9 (95.5-96.3)	83.8 (82.2-85.4)	0.876 (0.865-0.887)	0.989 (0.987-0.990)
DTI-SVM	High Tumor Cellularity	74.4 (73.4-75.4)	82.0 (81.5-82.6)	87.4 (0.86.8-0.88.0)	0.799 (0.790-0.808)	0.866 (0.861-0.872)
	Tumor Necrosis	62.3 (60.9-63.7)	95.9 (95.7-96.2)	78.8 (77.1-80.6)	0.677 (0.659-0.696)	0.934 (0.931-0.937)
	Tumor Infiltration	97.9 (97.7-98.1)	83.3 (82.4-84.3)	0.602 (58.1-62.3)	0.722 (0.705-0.739)	0.985 (0.984-0.987)

Table 1. Values were summarized as mean (95% Confidence Interval). TPR=true positive rate; TNR=true negative rate; PPV=positive predictive value; AUC=area under curve.